



Electrochemical properties of $\text{LiNi}_{1/3}\text{Co}_{1/3}\text{Mn}_{1/3}\text{O}_2$ cathode material modified by coating with Al_2O_3 nanoparticles



Kazuhiro Araki^{a,*}, Noboru Taguchi^b, Hikari Sakaebe^{b,**}, Kuniaki Tatsumi^b, Zempachi Ogumi^a

^a Office of Society-Academia Collaboration for Innovation, Kyoto University, Gokasho, Uji, Kyoto 611-0011, Japan

^b Research Institute for Ubiquitous Energy Devices, AIST, 1-8-31 Midorigaoka, Ikeda, Osaka 563-8577, Japan

HIGHLIGHTS

- We succeeded in suppressing the power fade using mechano-chemical bonding technology.
- Crack formation of NCM correlated with the ASI (10 s) increase.
- Coating with Al_2O_3 can be an effective technique for improving the power fade.

ARTICLE INFO

Article history:

Received 29 January 2014

Received in revised form

10 June 2014

Accepted 16 June 2014

Available online 25 June 2014

Keywords:

Lithium ion batteries

$\text{LiNi}_{1/3}\text{Co}_{1/3}\text{Mn}_{1/3}\text{O}_2$

Al_2O_3 coating

Nano particle

Mechano-chemical bonding technology

Crack

ABSTRACT

$\text{LiNi}_{1/3}\text{Co}_{1/3}\text{Mn}_{1/3}\text{O}_2$ particles were coated with Al_2O_3 nanoparticles by means of a mechanochemical bonding process; SEM confirmed that the Al_2O_3 particles were uniformly coated over the surface of the $\text{LiNi}_{1/3}\text{Co}_{1/3}\text{Mn}_{1/3}\text{O}_2$ powder. During subsequent electrochemical testing using pouch cells, uncoated $\text{LiNi}_{1/3}\text{Co}_{1/3}\text{Mn}_{1/3}\text{O}_2$ exhibited a gradual capacity fading and an increase in area specific impedance (ASI) at a 50% state of charge. Under the same conditions, the increase in ASI of the Al_2O_3 modified samples was significantly suppressed, although the initial performance (charge/discharge capacity and ASI) slightly deteriorated. The Al_2O_3 coating was also effective in improving the cyclability of $\text{LiNi}_{1/3}\text{Co}_{1/3}\text{Mn}_{1/3}\text{O}_2$ at elevated temperatures by reducing the extent of cracking.

© 2014 Elsevier B.V. All rights reserved.

1. Introduction

The recent emergence of hybrid and electric vehicles onto the market has highlighted the limitations of conventional lithium ion batteries in terms of their energy density, durability, electrochemical performance, and cost. As a result, $\text{LiNi}_{1/3}\text{Co}_{1/3}\text{Mn}_{1/3}\text{O}_2$ (NCM) has been considered as an alternative cathode material for such applications, as it offers a significant cost benefit over conventional LiCoO_2 . However, NCM also experiences appreciable degradation during cycling at elevated temperatures [1]. The use of

coatings is well known as an effective technique for improving the cyclability of positive active-materials at elevated temperatures and therefore several metal oxide coatings have been intensively studied for the surface modification of cathode materials, e.g., Al_2O_3 [2–5], ZrO_2 , MgO , and ZnO [6–9]; metal phosphates like AlPO_4 [10,11]; and metal fluorides like AlF_3 [12,13]. These techniques have been demonstrated to greatly enhance electrochemical properties, such as cyclability and rate capability, with Jung et al. reporting that these films can minimize Co dissolution or suppress surface reactions with the electrolyte [14]. Moreover, Cho et al. have shown that the expansion of the *c*-axis is sharply reduced during cycling, and that this results in negligible strain and microcrack formation [5]. However, the mechanism by which the cyclability is enhanced by this coating is still unclear, and subject to discussion.

In this work, (NCM) was coated with Al_2O_3 nanoparticles via a mechanochemical bonding technology [15] in order to investigate their effect on the electrochemical performance, surface characteristics, structure and morphology of NCM. By comparing these

* Corresponding author. Present address: Honda R&D Co., Ltd., 4630 Shimotakanazawa, Haga-machi, Haga-gun, Tochigi 321-3393, Japan. Tel.: +81 80 4871 4817; fax: +81 28 677 7460.

** Corresponding author. Tel.: +81 72 751 9673; fax: +81 72 751 9609.

E-mail addresses: kazuhiro_araki@n.t.rd.honda.co.jp (K. Araki), hikari.sakaebe@aist.go.jp (H. Sakaebe).

results with those of uncoated NCM, the mechanisms behind any observed improvement are discussed.

2. Experimental

A mechanochemical bonding process (AMS-MINI, Hosokawa Micron Corp.) was used to coat NCM (supplied by Toda Kogyo Corp.) 50 nm Al_2O_3 nanoparticles (Aldrich). This bonding process allows a variety of powders to be hybridized by a mechanochemical reaction that utilizes only mechanical energy; the basic principles and a schematic illustration of the essential components are shown in Fig. 1 [15]. In this process the powder is pressed against the inner wall of the rotor by centrifugal force, thus generating compressive and shear forces in the powder as it passes through the gap between the rotor and inner component. The amount of Al_2O_3 coated onto the NCM powders was 3.0 or 7.5 wt%, with Table 1 providing a detailed overview of the coating procedure.

The morphology of the powder particles was confirmed using a scanning electron microscope (SEM; S5000, Hitachi) and scanning-transmission electron microscope (STEM; Hitachi, S-5500). A cross-section polisher (E-3500, Hitachi) was used to prepare cross-sectional samples of the powder for imaging. Each electrode was held between two sheets of cover glass for microscope and cut by an argon-ion beam polisher at a constant power of 0.65 W (5 kV and 0.13 mA) under gas flow rate of 0.1 mL min^{-1} for 90 min. Oriented image mapping was reconstructed from an electron backscatter diffraction (EBSD) pattern (TSL Solutions KK). For this, the electron beam was scanned over the sample, with the EBSD pattern measured at each point then indexed to ascertain the orientation of the crystal lattice. A high-speed CCD camera (1500M-T1-GE-EX) and the software package TSL OIM Data Collection 6 were used for the pattern acquisition and mapping image reconstruction, respectively. X-ray diffractometry (XRD; Rigaku, RINT 2200) was employed to characterize the crystal structure of the powder sample. XRD data were obtained using Cu $K\alpha$ radiation ($\lambda = 0.15406 \text{ nm}$) in continuous scan mode across a 2θ range of $10\text{--}80^\circ$, with a step size of 0.02° and a scan rate of 2° per minute. X-ray photoelectron spectroscopy (XPS, ULVAC-PHI QuanteraSXM with Al $K\alpha$ radiation, $h\nu = 1486.71 \text{ eV}$) measurements (about $\phi 100 \mu\text{m}$) were performed to investigate the surface of the electrodes before and after cycling. For this, all cells were first disassembled in a dry box filled with argon gas in which the dew point was below -50°C . Next, the electrodes were washed with diethyl carbonate (DEC), dried, and then transported for analysis under an inert atmosphere. Physical properties were assessed using a microcompression testing machine (MCT-510, Shimadzu) with a $50 \mu\text{m}\phi$ flat indenter (load: 9.8–55 mN, displacement: 0–100 μm) to determine the compressive strength. Tensile strength was also obtained from the load–displacement curve.

Electrochemical performance was evaluated using pouch-type full cells (49 cm^2) in which the positive electrode consisted of 90 wt% coated or uncoated NCM combined with 5 wt% of carbon

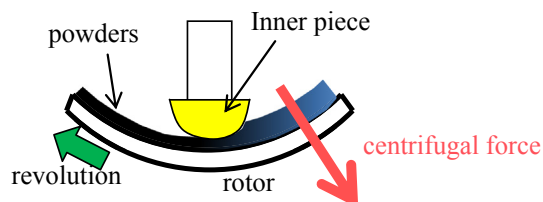


Fig. 1. Schematic illustration of the primary components of a Hosokawa mechanochemical bonding coating device [15].

Table 1
Process of coating Al_2O_3 nanoparticles onto NCM-10.

Step no.	Step rotation number (rpm)	Step time (min.)	3.0 wt% Al_2O_3	7.5 wt% Al_2O_3
1	4000	1	mixing of 81 g NCM, with 1.250 g Al_2O_3	mixing of 81 g NCM, with 1.312 g Al_2O_3
2	4000	1	adding 1.250 g Al_2O_3	adding 1.312 g Al_2O_3
3	4000	1		adding 1.312 g Al_2O_3
4	4000	1		adding 1.312 g Al_2O_3
5	4000	1		adding 1.312 g Al_2O_3

black (Super-P(Li), TIMCAL) and 5 wt% of polyvinylidene fluoride (PVDF) (KLF#1120, Kureha). The negative electrode consisted of 93 wt% hard-carbon (Carbotron-P(J), Kureha) and 7 wt% PVDF (KLF#9130, Kureha). All electrodes were dried under vacuum at 160°C for 12 h prior to cell assembly. For the assembly, a porous polypropylene membrane (#2500, Celgard) was used as a separator and 1.0 mol dm^{-3} LiPF_6 /ethylene carbonate-dimethyl carbonate-ethylmethyl carbonate (1:1:1 by volume) served as the electrolyte. A three-electrode electrochemical cell was also assembled to compare the potential of uncoated positive and negative electrodes, in which a Li reference electrode was inserted in between the electrodes of the cell. Assembly of all cells was carried out in a dry room, after which they were charged and discharged for three cycles at a rate of 1C within a voltage range of 4.2–2.7 V at 25°C using a multi-channel charge–discharge device (TOSCAT-3000, Toyo System Co., Ltd.). The area specific impedance (ASI) was evaluated at a 50% state of charge (SOC), which corresponds to a cell voltage of 3.615 V. ASI was measured at 3, 5, 8 and 12C for 12 s at each pulse current rate rest for 10 min in order to attain linearity at room temperature, following the previously reported procedure [18]. The voltage after 1 or 10 s (V_{1s} or V_{10s}) was recorded at each current pulse, and plots of V_{1s} – I and V_{10s} – I were obtained in which (I) corresponds to the absolute current for each pulse. The each decision coefficient is over 0.999 on the slopes of the V_{1s} – I and V_{10s} – I . The state of relaxation of the cell has a small influence on the V – I plots under our experimental conditions. The absolute values of the slopes of these V – I plots, as normalized by the electrode area, were used to determine the ASI values at 10 and 1 s intervals, which are hereafter denoted as ASI(10s) and ASI(1s), respectively. The rate capability was tested by discharging at current densities of 1, 5, 10, 20, 30 and 50C. Cycling performance was evaluated in the voltage range of 2.7–4.2 V using a constant current/constant voltage (CC/CV) method for charging to 4.2 V with a typical test current of 110 mA g^{-1} , and a CC method for discharging to 2.7 V with a typical test current of 110 mA g^{-1} at 50°C . Monitoring of the discharge capacity, ASI(10s) and ASI(1s) was conducted at 25°C for 100 and 250 cycles.

3. Results and discussion

Fig. 2 shows SEM images of the surfaces of uncoated and coated NCM particles. From this, we can see that the concave regions are the first to be filled with coating material, with the convex parts only being covered when the amount of coating is increased. Thus, the enclosed section corresponding to the convex region of NCM was apparently less covered in the case of 3.0 wt% coated particles (Fig. 2(b)), whereas the surface of the 7.5 wt% coated particles was so completely covered by Al_2O_3 nanoparticles that the morphology of the original uncoated particle could no longer be seen (Fig. 2(c)). Fig. 2(d) shows a cross-sectional STEM image of the surface region of the particle coated by 7.5 wt% Al_2O_3 , in which the thickness of coating can be seen to vary from 150 to 300 nm.

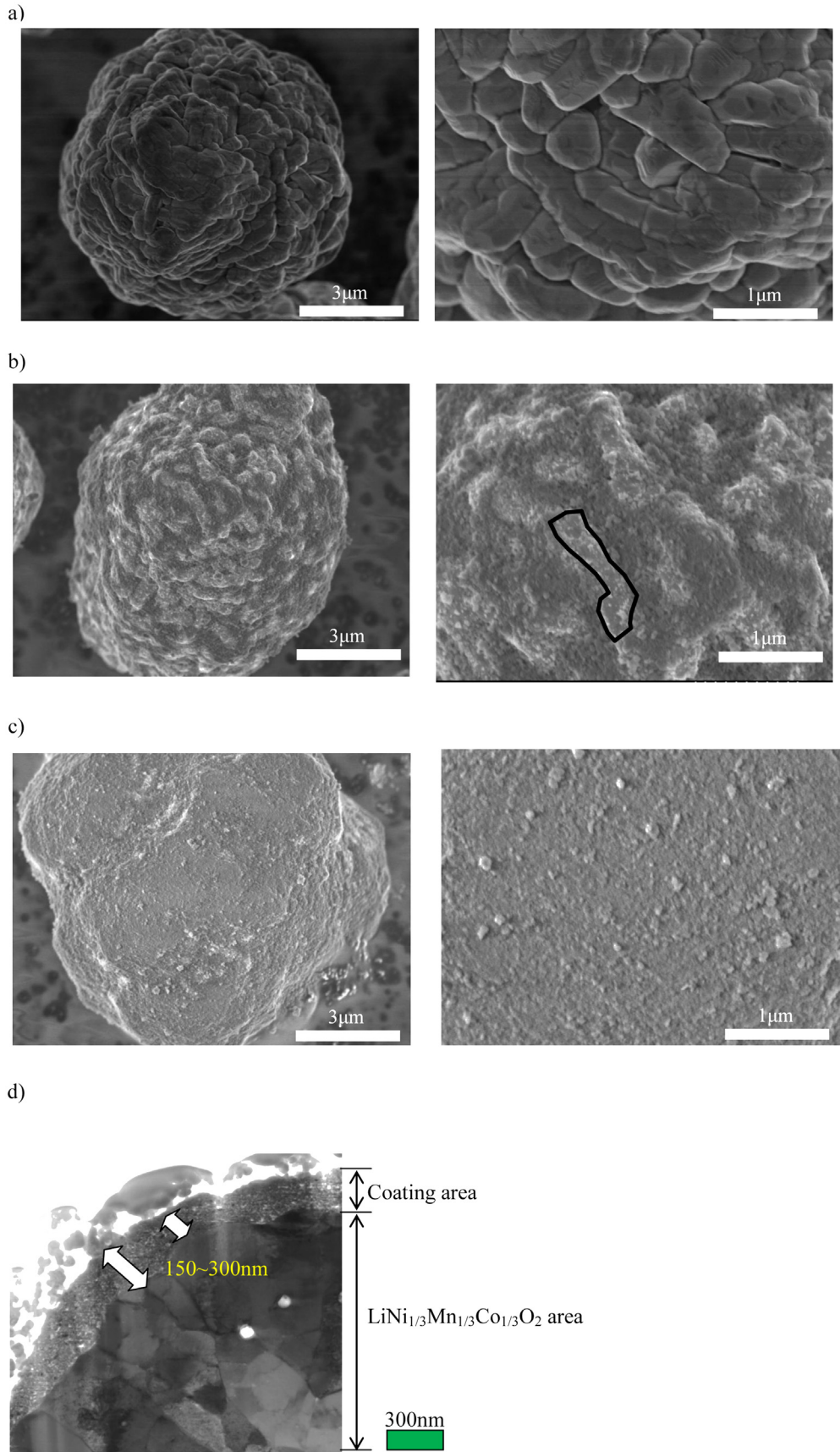


Fig. 2. SEM and TEM images of $\text{LiNi}_{1/3}\text{Co}_{1/3}\text{Mn}_{1/3}\text{O}_2$ powder (a) uncoated, (b) coated with 3.0 wt% Al_2O_3 , and (c) coated with 7.5 wt% Al_2O_3 . (d) Cross-sectional STEM image of the particle in (c).

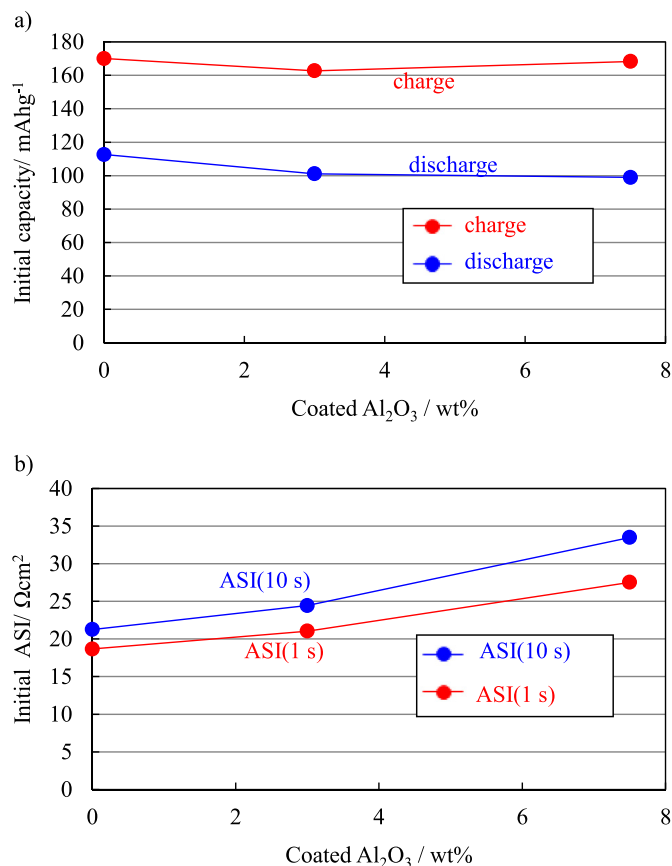


Fig. 3. Correlation between the initial electrochemical performance at 25 °C of coated/uncoated LiNi_{1/3}Co_{1/3}Mn_{1/3}O₂ and (a) charge/discharge capacity and (b) area specific impedance ASI(10 s) and ASI(1 s).

Fig. 3 illustrates the correlation between the initial charge/discharge capacity and area specific impedance (ASI) with Al₂O₃ loading. In this, the full cell was charged at a current density of 22 mA g⁻¹ (0.2C-rate) up to 4.2 V, revealing that the discharge capacity of the coated sample undergoes a perceptible capacity loss. Furthermore, the initial ASI(10s) and ASI(1s) is gradually increased with Al₂O₃ loading, which can be ascribed to a decrease in contact area between each active material particle, and also between particles of active material and carbon black.

A comparison of the rate capabilities of uncoated, 3.0 and 7.5 wt % Al₂O₃-modified NCM is shown in Fig. 4. This shows that the

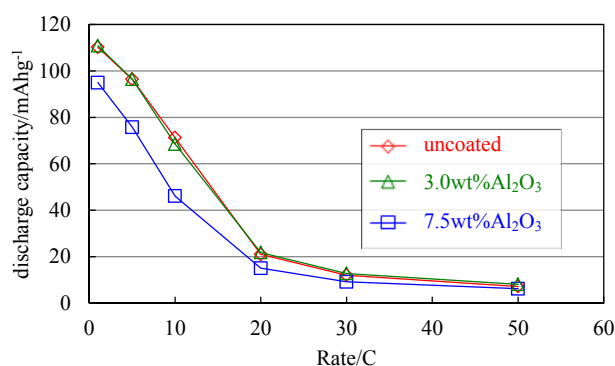


Fig. 4. Rate capability of \diamond uncoated, \triangle 3.0 wt% Al₂O₃-coated, and \square 7.5 wt% Al₂O₃-coated samples.

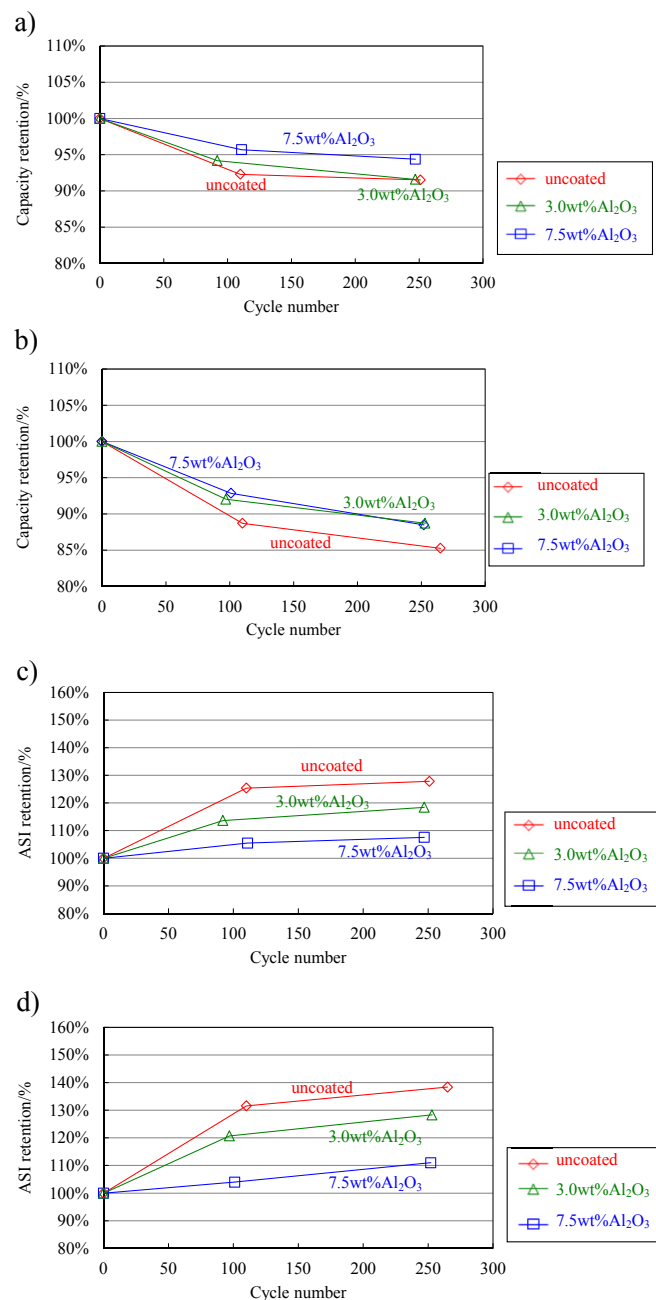


Fig. 5. Cycling performance of coated/uncoated samples. (a) Capacity retention during cycling at 35 °C, (b) capacity retention during cycling at 50 °C, (c) ASI(10s) ratio during cycling at 35 °C, and (d) ASI(10s) ratio during cycling at 50 °C.

capacity of uncoated NCM at 10C is 71 mAh g⁻¹, which corresponds to about 65% of that at 1C. In contrast, the capacity of 3 wt% Al₂O₃-coated NCM is 68.5 mAh g⁻¹ at 10C, or about 62% of that at 1C, whereas the capacity at 7.5 wt% Al₂O₃ of 46.1 mAh g⁻¹ at 10C corresponds to only about 49% of that at 1C. This obvious difference in the rate capability of the 7.5 wt% Al₂O₃-modified NCM is most likely caused by the reduced contact area between the conductor and the active materials.

Fig. 5 shows the dependency of capacity retention and ASI(10s) of cells containing coated samples on the number of cycles. These results clearly indicate that Al₂O₃ modification suppresses the increase in ASI(10s) with cycling, and although the capacity retention gradually decreased with an increasing number of cycles, the rate of

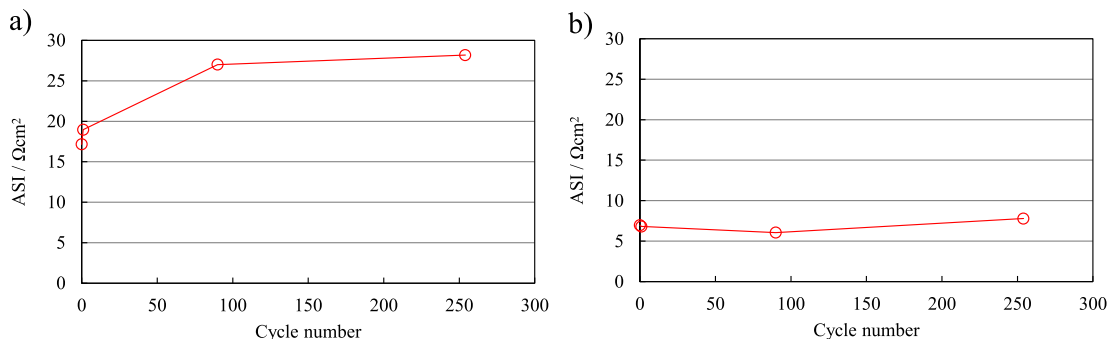


Fig. 6. Increase in ASI(10s) of a three-electrode electrochemical cell containing (a) an uncoated positive electrode and (b) a negative electrode.

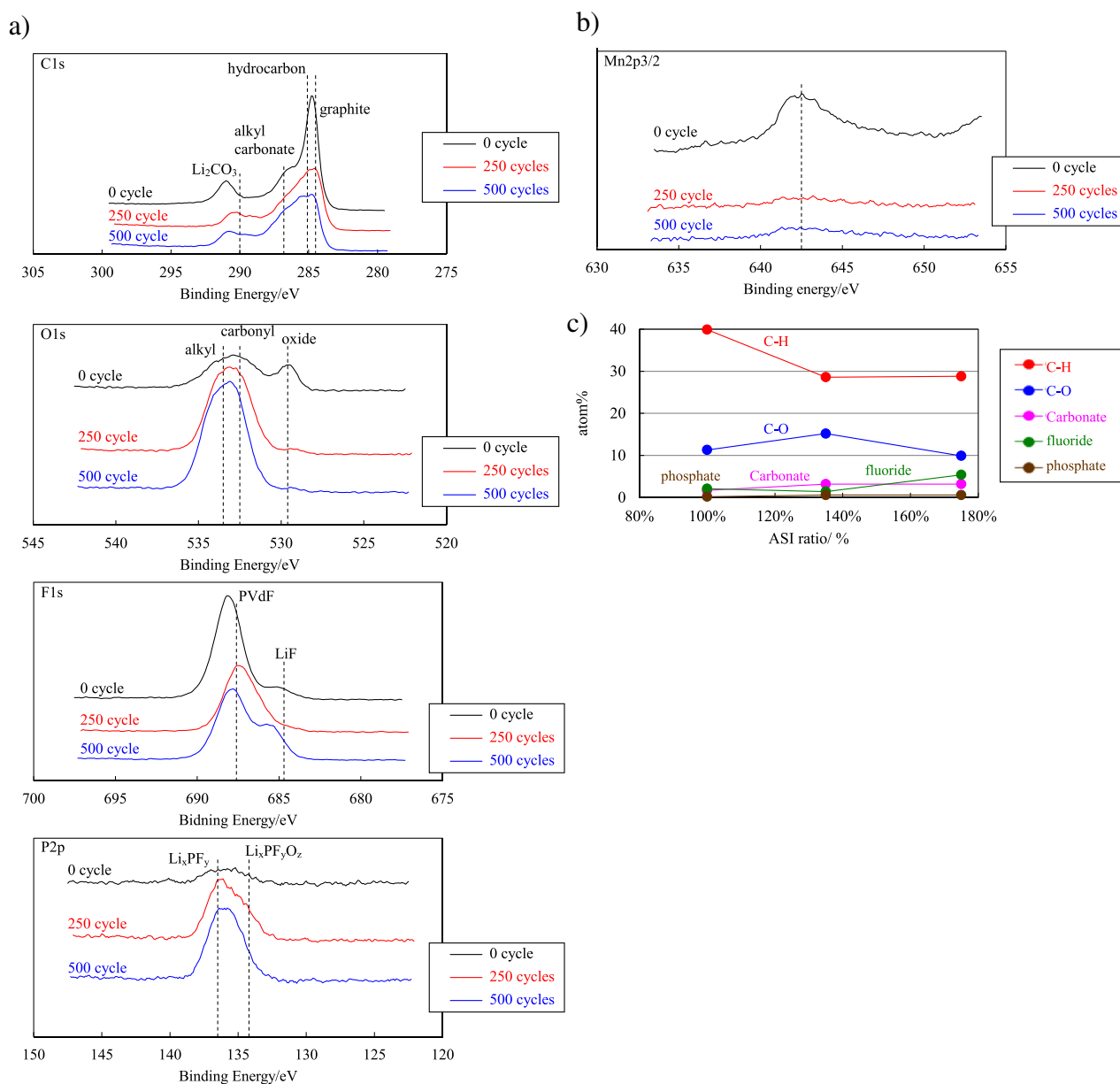


Fig. 7. XPS correlation of degradation (a) XPS spectra of an uncoated sample after 0, 250 and 500 cycles on a positive electrode, (b) XPS spectra of an uncoated sample after 0, 250 and 500 cycles on a negative electrode, (c) ratio of SEI compounds on a positive electrode.

Table 2

Concentration of Mn on the negative electrode surface, as determined by the peak area ratio of Mn 2p_{3/2} spectrum to the total area of detected elements.

Sample	ASI(10s) ratio (%)	Mn (at%)
Fresh	100%	0.1%
35 °C, 250 cycles	122%	0.6%
50 °C, 250 cycles	135%	0.6%
50 °C, 250 cycles	175%	0.8%

decrease did not significantly differ between uncoated and coated samples.

The electrochemical behavior of the uncoated and 7.5 wt% coated positive and negative electrodes was examined in detail using a three-electrode cell at 50 °C. Through this, a change in the ASI(10s) was observed at 25 °C after the 100th and 250th cycles, as illustrated in Fig. 6. This increase in the ASI(10s) is attributed mainly to the increase of the positive electrode, with the Al₂O₃ coating effectively suppressing the ASI(10s) increase with degradation.

XPS analysis was used to identify the chemical species present on the surface of the electrodes by comparing the peaks obtained against those identified in the literature [19,20]. In the O_{1s} spectra (Fig. 7(a)), a small signal attributable to metal oxide is clearly discernible at 529.6 eV in each cycled sample. The peaks at 532.5 and 533.5 eV correspond to carbonyl oxygen and oxygen for alkyl group, respectively. In the P_{2p} spectra (Fig. 7(a)), the peaks for Li_xPF_y at 136.5 eV and Li_xPF_yO_z at 134.2 eV are both clearly evident. It can therefore be inferred from these results that by cycling at 50 °C, a solid electrolyte interphase (SEI) film is produced that covers the surface of the active material. Moreover, the Mn 2P_{3/2} spectra (Fig. 7(b)) of the negative electrodes suggest the presence of a Mn compound at 642.5 eV with increased cycles [21]. We therefore looked at the area ratio of the decomposition products of the electrolyte (C–H and C–O signals from carbonate, fluoride, and phosphate signals) on the positive electrode, and the Mn species originating from NCM that were deposited on the negative electrode. Fig. 7(c) shows the correlation in intensity of these peaks from the surface of the positive electrode and the ASI ratio, indicating that none of the chemical species from the SEI has a close relationship with the ratio of ASI(10s). Furthermore, the results shown in Table 2 indicate that the atomic concentration of Mn on

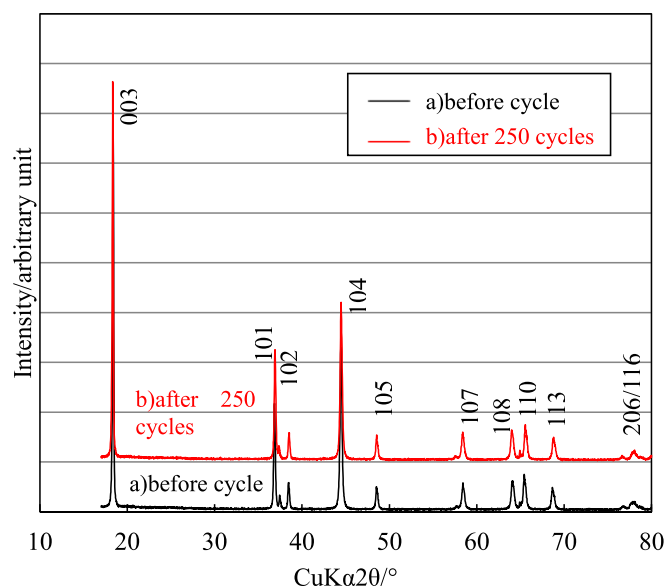


Fig. 8. XRD patterns for an electrode (a) before cycling, and (b) after 250 cycles.

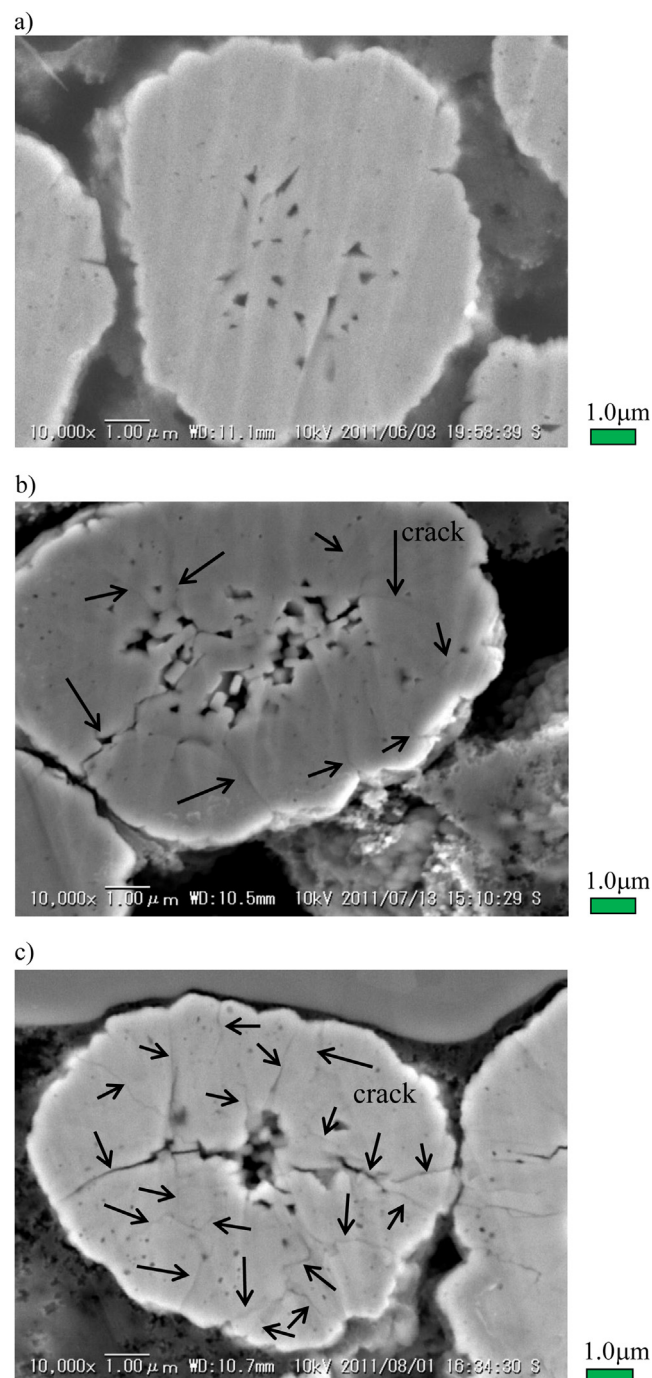


Fig. 9. Cross-sectional SEM images of uncoated electrodes (a) before cycling, (b) after 100 cycles with an ASI(10s) ratio of 121%, and (c) after 250 cycles with an ASI(10s) ratio of 128%.

the negative electrode of ASI(10s) at ratios of 122 and 135% was the same. Since it is well-known that the charge compensation and oxygen vacancy mechanism drives Mn dissolution, resulting in the reduction of Mn⁴⁺ to Mn³⁺ in positive active materials [22], it seems likely that the Mn ions migrating to the negative electrode are deposited on the surface of the carbon. This phenomenon degrades cell performance, and so if Mn dissolution is indeed responsible for the ASI(10s) degradation then we would expect there to be more Mn in the cell with the higher ASI(10s) ratio. The fact that the observed results deviate from this expectation

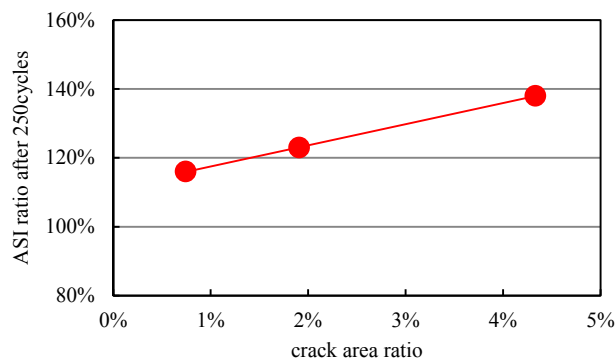


Fig. 10. Correlation between ASI(10s) ratio and crack area ratio in uncoated positive electrode particles.

suggests that Mn dissolution can not be a significant factor in degradation.

To evaluate any change in the bulk structure, the XRD patterns of electrodes before and after 250 cycles were compared (Fig. 8). In this, both the original and cycled uncoated electrode can be identified as a layered α -NaFeO₂ structure, with a space group of R-3m. The calculated cell parameters were $a = b = 2.84$ Å and $c = 14.36$ Å. Although the detailed cell parameters differed slightly due to the use of a 2-electrode full cell, no additional peaks were found in the electrode after cycling. The bulk structure was also found to have no significant relationship with the observed degradation.

Fig. 9 shows a cross-sectional image of a representative single-particle in a cycled positive-electrode (uncoated NCM) of a three-electrode cell. In this, the cracks (indicated by arrows) can be seen to increase dramatically with cycling. Fig. 10 illustrates the dependence of ASI(10s) on the crack area ratio, which is defined as the ratio of cracks/total area of the particle as calculated by image processing techniques. It is evident from this that the area of cracks inside particles shows a clear correlation with ASI(10s) in the uncoated positive electrode of the three-electrode cell. It should also be noted that this crack area ratio was estimated from 10 representative particles of an SEM view containing more than 40 particles in total. Itou et al. have suggested that in the case of LiNi_{0.8}Co_{0.15}Al_{0.05}O₂ the degradation mechanism of the positive electrode is an increase of resistance caused by morphological change of the particles [16]. With this in mind, it can be concluded

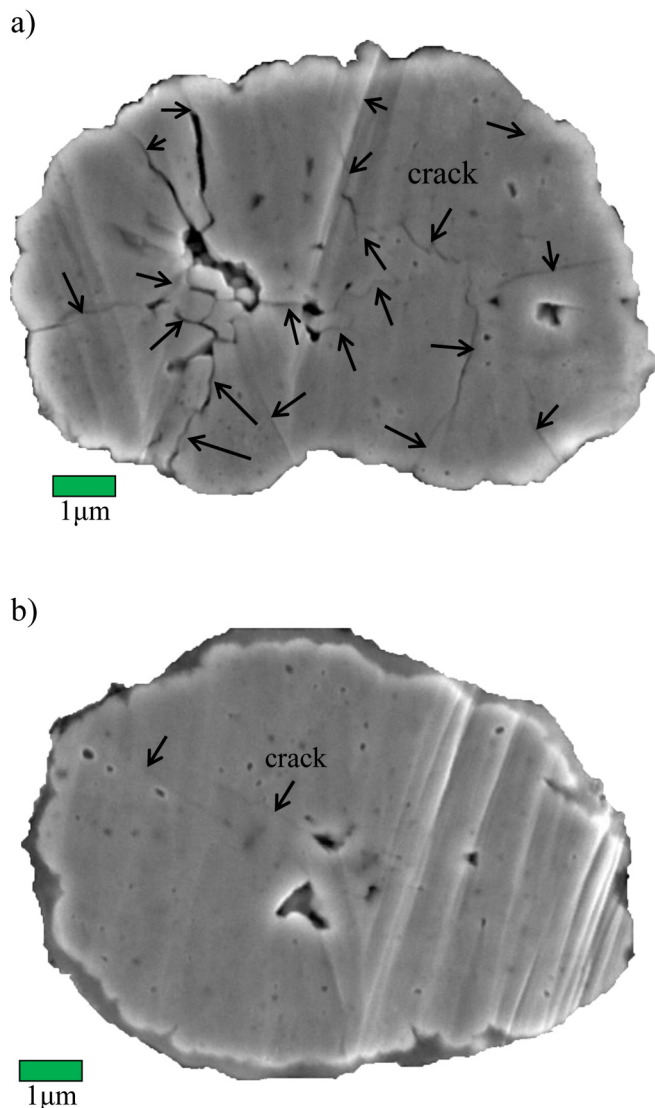


Fig. 12. Cross-sectional SEM images of electrodes cycled 250 times at 50 °C: (a) uncoated and (b) 7.5 wt% Al₂O₃ coated.

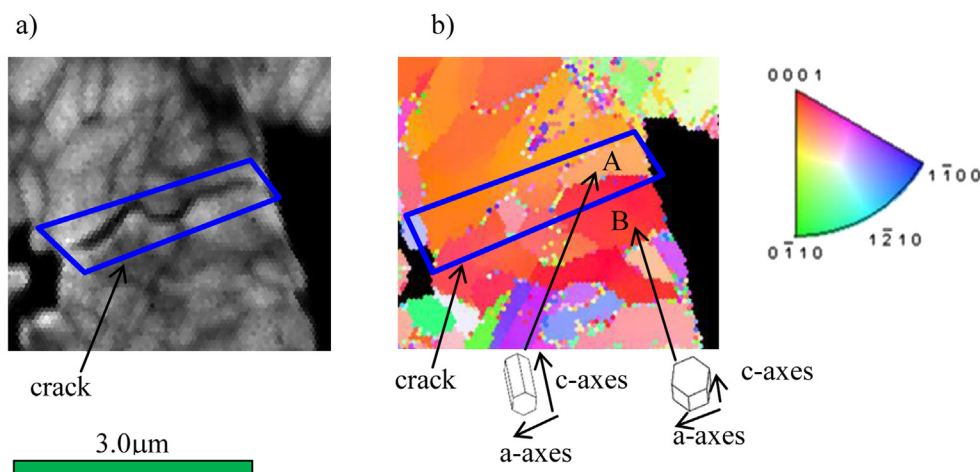


Fig. 11. Backscatter electron images of ground sections of cracks in an uncoated particle cycled 250 times at 50 °C: (a) SEM image and (b) EBSD image.

Table 3Strength of uncoated and 7.5 wt% Al₂O₃-coated NCM particles.

Sample	Particle strength (MPa)
Uncoated NCM	128
NCM coated by 7.5 wt% Al ₂ O ₃	168

that the increase in ASI(10s) is caused by increasing evolution of cracks leading to degradation of the electrochemical properties.

Since the reason why these cracks increase is very important, the internal structure of the particles was investigated further using EBSD. Fig. 11 shows an EBSD image of uncoated NCM particles after 250 cycles, in which the different colors represent different crystal orientations. The figure shows that the primary particles facing the notch, for example in the boxed area, are in a different crystal orientation. The crystal *c*-axes of primary particles A and B are almost mutually orthogonal. The lattice parameters are changed to a completely opposite direction during the charge/discharge process, and the stress concentrated at the grain boundary of two primary particles during such a change is the most likely cause of cracking.

Fig. 12 shows cross-sectional images of coated and non-coated NCM after 250 cycles at 50 °C, each image indicating a representative secondary particle from an SEM view containing more than 40 particles. The ASI ratios of uncoated NCM and NCM coated with 7.5 wt% Al₂O₃ were 138 and 111%, respectively. Thus, for a given number of cycles, it is clear that the number of cracks in coated NCM is dramatically less than that of an uncoated sample.

Cho et al. reported that a thin-film coating of high-fracture-toughness oxides suppresses the *c*-axis expansion (or phase transition) of LiCoO₂, thereby preventing capacity fading during electrochemical cycling [17]. In contrast, Itou et al. reported that occurrence of cracking in LiNi_{0.8}Co_{0.15}Al_{0.05}O₂ was one of the factors in its increased resistance [16]. The particle strengths of the uncoated and coated samples were therefore measured using a microcompression testing machine. The results in Table 3 indicate that the average particle strength of coated particles is slightly higher than that of uncoated NCM. We can speculate from this enhancement of particle strength that the suppressed cracking during the charge/discharge cycle is at least one factor in determining capacity fade, but that other factors need to be taken into account.

4. Conclusions

This study has revealed that the increase of ASI in an NCM-based cell is due to the increased ASI of the active material at the positive electrode, which in turn is caused by the formation of cracks in

secondary particles. We succeeded in suppressing this increase of ASI by coating NCM with Al₂O₃ nanoparticles using a mechano-chemical bonding technology. This confirmed that crack formation inside the secondary particles of NCM correlates to the ASI increase. Moreover, the Al₂O₃ nanoparticle coating enhanced the particle strength, and this contributed to reducing the degree of crack growth inside the particles. Coating with Al₂O₃ therefore provides an effective technique for improving the life and power fade of Li-ion cells that utilize NCM as the positive electrode material.

Acknowledgments

This work was financially supported by the “Research & Development Initiative for Scientific Innovation of New Generation Batteries (RISING)” project of the New Energy and Industrial Technology Development Organization (NEDO).

References

- [1] K. Amine, Z. Chen, Z. Zhang, J. Liu, W. Lu, Y. Qin, J. Lu, L. Curtis, Y. Sun, J. Mater. Chem. 21 (2011) 17754–17759.
- [2] Y. Huang, J. Chen, F. Cheng, W. Wan, W. Liu, H. Zhou, X. Zhang, J. Power Sources 195 (2010) 8267–8274.
- [3] S. Park, S. Lee, W.I. Cho, B.W. Cho, Met. Mater. Int. 16 (1) (2010) 93–98.
- [4] L. Liu, L. Chen, X. Huang, X. Yang, W. Yoon, H.S. Lee, J. McBreen, J. Electrochem. Soc. 151 (2004) A1344–A1351.
- [5] J. Cho, Y.J. Kim, B. Park, Chem. Mater. 12 (2000) 3788–3791.
- [6] Y. Huang, J. Chen, J. Ni, H. Zhou, X. Zhang, J. Power Sources 188 (2009) 538–545.
- [7] S. Hu, G. Cheng, M. Cheng, B. Hwang, R. Santhanam, J. Power Sources 188 (2009) 564–569.
- [8] B.J. Hwang, C.Y. Chen, M.Y. Cheng, R. Santhanam, K. Ragavendran, J. Power Sources 195 (2010) 4255–4265.
- [9] G.Q. Liu, H.T. Kuo, R.S. Liu, C.H. Shen, D.S. Shy, X.K. Xing, J.M. Chen, J. Alloys Compd. 496 (2010) 512–516.
- [10] Y. Cho, J. Eom, J. Cho, J. Electrochem. Soc. 157 (2010) A617–A624.
- [11] J.Y. Shi, C. Yi, K. Kim, J. Power Sources 195 (2010) 6860–6866.
- [12] S.-U. Woo, C.S. Yoon, K. Amine, I. Belharouak, Y.-K. Sun, J. Electrochem. Soc. 154 (2007) A1005–A1009.
- [13] S. Lee, C.S. Yoon, K. Amine, Y. Sun, J. Power Sources 234 (2013) 201–207.
- [14] Y.S. Jung, A.S. Cavanagh, A.C. Dillon, M.D. Groner, S.M. George, S. Lee, J. Electrochem. Soc. 157 (2010) A75–A81.
- [15] A.D. Pasquier, C.C. Huang, T. Spitler, J. Power Sources 186 (2009) 508–514.
- [16] Y. Itou, Y. Ukyo, J. Power Sources 146 (2005) 39–44.
- [17] J. Cho, Y.J. Kim, T. Kim, B. Park, Angew. Chem. Int. 40 (18) (2001) 3367–3369.
- [18] H. Kobayashi, M. Shikano, S. Koike, H. Sakaebe, K. Tatsumi, J. Power Sources 174 (2007) 380–386.
- [19] A.M. Andersson, D.P. Abraham, R. Haasch, S. Maclaren, L. Liu, K. Amine, J. Electrochem. Soc. 149 (2002) A1358–A1369.
- [20] N. Dupré, J.-F. Martin, J. Oliveri, P. Soudan, A. Yamada, R. Kanno, D. Guyomard, J. Power Sources 196 (2011) 4791–4800.
- [21] M. Shikano, H. Kobayashi, S. Koike, H. Sakaebe, Y. Saito, H. Hori, H. Kageyama, K. Tatsumi, J. Power Sources 196 (2011) 6881–6883.
- [22] Z. Lu, D.D. MacNeil, J.R. Dahn, Electrochem. Solid State Lett. 4 (2001) A191–A194.